From models to mechanisms: defects and charge trapping in amorphous silicon nitride

Hückmann, L.

2

Theory and Methods

The solid state of matter comprises materials whose constituent atoms, ions, or molecules are held together by cohesive forces strong enough to maintain structural integrity at a given temperature. Solids are broadly classified into *crystalline* and *amorphous* materials. Crystalline solids exhibit a three-dimensionally periodic, long-range ordered structure, whereas amorphous materials are primarily characterized by the absence of such order. As outlined in Chapter 1, this thesis focuses on the amorphous dielectric Si-based materials used in electronic devices. However, to systematically study amorphous systems, it is essential to understand the theoretical framework developed for crystalline solids, since many of the concepts and models applied here originate from crystalline theory.

This chapter is structured as follows: In Section 2.1, a brief introduction to crystal structures and terminology used throughout this thesis is provided. This is followed by an overview of the theoretical approaches used to describe atomic interactions, beginning with classical interatomic potentials in Section 2.2 and the foundations of density functional theory (DFT) in Section 2.3. Finally, Section 2.4 outlines the practical implementation of DFT in the form of the Gaussian and Plane Wave (GPW) method and Section 2.5 discusses considerations on the modeling of defects in solids. In addition to the references cited in the respective sections of the text, this chapter was created with the books provided in References [1–6].

2.1 Description of Solids

2.1.1 The Structure of Crystals

A crystal is defined as a solid whose atoms are arranged periodically in all three spatial directions and, therefore, they exhibit long-range order and obey to a certain symmetry.[6] In such a structure, there is a smallest set of atoms that can be periodically repeated to build up the entire crystal. This set of atoms is referred to as the *basis*. Mathematically, such an arrangement is expressed by a point lattice where any arbitrary lattice position $p(\boldsymbol{r})$ has infinitely equivalent ones that can be mapped onto each other *via* translation along the vector $\boldsymbol{R}$ according to

$$p(\boldsymbol{r}) = p(\boldsymbol{r} + \boldsymbol{R}) \tag{2.1}$$

where the translation vector $\boldsymbol{R}$

$$\boldsymbol{R} = n_1\boldsymbol{a} + n_2\boldsymbol{b} + n_3\boldsymbol{c}\,, \quad n_1, n_2, n_3 \in \mathbb{Z} \quad . \tag{2.2}$$

is an integer linear combination of the basis vectors $\boldsymbol{a}$, $\boldsymbol{b}$, $\boldsymbol{c}$ spanning a parallelepiped with the angles α, β, γ. The edge lengths a, b, c are referred to as *lattice constants*. Strictly speaking, there is more than one representation for a point lattice in a crystal, since any number of parallelepipeds that fulfill the boundary conditions can be constructed. This is why, in practice, the so-called *conventional unit cell* is usually used, which is defined as the smallest possible cell that exhibits the same symmetry elements as the crystal structure (in particular

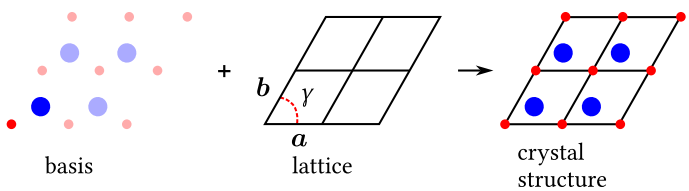

Figure 2.1: A fictitious example of a 2D crystal to illustrate the basis atoms and the point lattice with the basis vectors $\boldsymbol{a}$ and $\boldsymbol{b}$ that describe the crystal structure.

the multiplicity of the principle axis of rotation, see below). By taking into account that the unit cell must completely fill space and must not overlap upon translation by the lattice vectors, it can be shown that there are only seven distinguishable *crystal systems*. The volume of the unit cell is simply given by

$$V = \boldsymbol{a}\,(\boldsymbol{b} \times \boldsymbol{c}) \quad . \tag{2.3}$$

This concept is illustrated in Figure 2.1 with a 2D example. In the simplest case, the basis is comprised of a single atom, which is referred to as a primitive (P) lattice. As displayed in Figure 2.1, this is not the case for all crystals. These non-primitive cells can be grouped in base-centered (B), body-centered (I), and face-centered (F) lattices. However, not every crystal system can encompass any non-primitive cell. In fact, the French mathematician Auguste Bravais proved that only seven primitive and seven non-primitive lattices exist in three-dimensional space, which are referred to as the 14 *Bravais lattices*.[7,8]

Besides translational symmetry, unit cells exhibit point symmetry,[9] *i.e.,* rotation, reflection, improper rotation, and inversion. Commonly, the symmetry elements are denoted following the Hermann-Mauguin[10,11] notation with n for rotation axes, m for mirror planes, and $\bar{n}$ for improper rotations. Here, n is the multiplicity of the rotation axis resulting from the rotational angle $2\pi/n$. Since unit cells must fill space without gaps and without overlapping, only 1-, 2-, 3-, 4-, and 6-fold rotations are feasible in three-dimensional space. For reflection planes, it can be further distinguished between being orthogonal or parallel to the principle axis of the unit cell denoted as $\frac{n}{m}$ and m, respectively. As a result of group theory, some symmetry operations exclude each other, are identical, or do not comply with the translational symmetry of the lattice. There is a finite amount of point groups compatible with a crystal system, such that the latter can be divided further into 32 *crystal classes*.

2.1.2 The Reciprocal Lattice

The inherent periodicity of an ideal crystal suggests expanding the properties of the unit cell in Fourier space, where the spectral representation conveniently describes diffraction phenomena as well as the motion of (quasi-)particles in a periodic potential.[5] In general,

the Fourier series of a function $f(\boldsymbol{r})$ defined on the real-space lattice can be written as

$$f(\boldsymbol{r}) = \sum_{hkl} f_{hkl} e^{i\boldsymbol{G}_{hkl}\boldsymbol{r}} \tag{2.4}$$

where the vectors $\boldsymbol{G}$ are the reciprocal lattice vectors characterized by the integers h, k, l. These vectors preserve the lattice periodicity by $\exp(i\boldsymbol{G}_{hkl}\boldsymbol{R}) = 1$ when $\boldsymbol{G}_{hkl}\boldsymbol{R} = 2\pi N$ with $N \in \mathbb{Z}$, which is the defining property for the vectors $\boldsymbol{G}$. Analogous to the real-space lattice introduced in Equation 2.2, the set of all $\boldsymbol{G}_{hkl}$ forms the reciprocal lattice

$$\boldsymbol{G}_{hkl} = h\tilde{\boldsymbol{a}} + k\tilde{\boldsymbol{b}} + l\tilde{\boldsymbol{c}} \tag{2.5}$$

which can be constructed from the real-space lattice vectors $\boldsymbol{a}$, $\boldsymbol{b}$, $\boldsymbol{c}$. In three dimensions, the basis vectors of the reciprocal lattice $\tilde{\boldsymbol{a}}$, $\tilde{\boldsymbol{b}}$, $\tilde{\boldsymbol{c}}$ are given by

$$\tilde{\boldsymbol{a}} = \frac{2\pi}{V}(\boldsymbol{b} \times \boldsymbol{c}) \tag{2.6}$$

$$\tilde{\boldsymbol{b}} = \frac{2\pi}{V}(\boldsymbol{c} \times \boldsymbol{a}) \tag{2.7}$$

$$\tilde{\boldsymbol{c}} = \frac{2\pi}{V}(\boldsymbol{a} \times \boldsymbol{b})\,. \tag{2.8}$$

with the unit cell volume $V = \boldsymbol{a}\,(\boldsymbol{b} \times \boldsymbol{c})$. By construction, the two sets of basis vectors satisfy the orthogonality relation

$$\boldsymbol{a}_i \cdot \tilde{\boldsymbol{a}}_j = 2\pi\delta_{ij}\,. \tag{2.9}$$

A key concept arising from the reciprocal lattice is the *Brillouin zone* (BZ), defined as the Wigner–Seitz cell in reciprocal space. The first Brillouin zone is the area in k-space that is closer to the origin than to any other reciprocal lattice point, see Figure 2.2. By construction, it contains all unique wavevectors needed to describe the periodicity of the crystal, making it the fundamental domain for electronic and vibrational states. Any Bloch function or plane-wave expansion can be restricted to wavevectors within the first Brillouin zone, since wavevectors outside this region can be translated back by a reciprocal lattice vector without altering the physics. Consequently, the Brillouin zone plays a central role in electronic structure calculations, including density functional theory, as it determines the minimal set of k-points required to sample the infinite periodic solid.

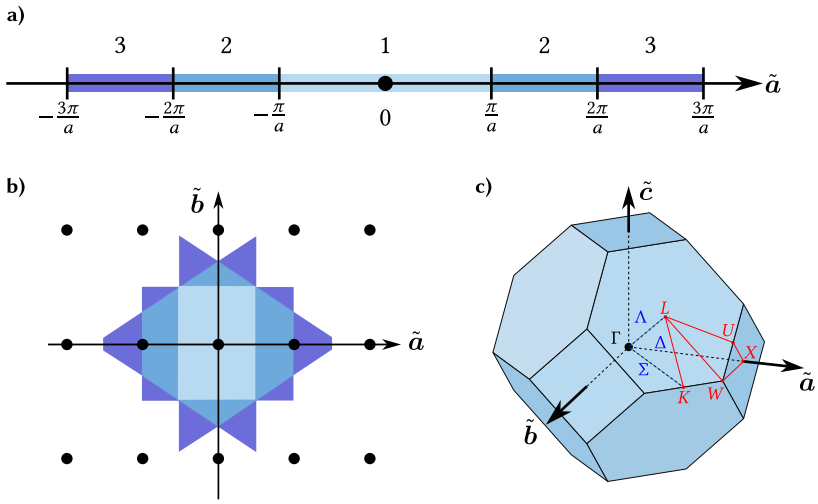

Figure 2.2: Depiction of the Brillouin zone of a) a hypothetical one-dimensional chain of atoms with the lattice constant a, b) a hypothetical two-dimensional rectangular grid, and c) of a cubic FCC lattice with the high-symmetry point Γ, K, L, W, U, and X. Adapted from Reference [5].

Within the Brillouin zone, certain points and lines possess higher symmetry than others, meaning that they are invariant under multiple lattice symmetry operations. These are referred to as high-symmetry points (*e.g.*, Γ, K, L, W, U, and X in the FCC lattice) and high-symmetry paths connecting them. They are of particular importance in electronic structure calculations because band extrema, degeneracies, and key features of the dispersion relations often occur at or along these points and paths. For disordered or large supercell systems, the first Brillouin zone becomes correspondingly small, and often sampling at the Γ-point alone provides a good approximation of the electronic structure.

2.1.3 Crystalline Phases of Silicon Nitride (Si_3N_4)

Silicon nitride crystallizes in three different phases: α-Si_3N_4, β-Si_3N_4, and γ-Si_3N_4. The α- and β-phase are structurally similar, differing only in the occurrence of one mirror plane. Dopants and impurities seem to play a pivotal role in stabilizing the α-phase, resulting in an ongoing debate whether the α-phase is to be considered an independent modification.[12–14] The γ-phase is a cubic high-pressure modification.[15] For these reasons, only β-Si_3N_4 is being considered when properties of the amorphous and crystalline phase are being compared. β-Si_3N_4 crystallizes in a hexagonal lattice with space group $P6_3/m$ (No. 176), containing two

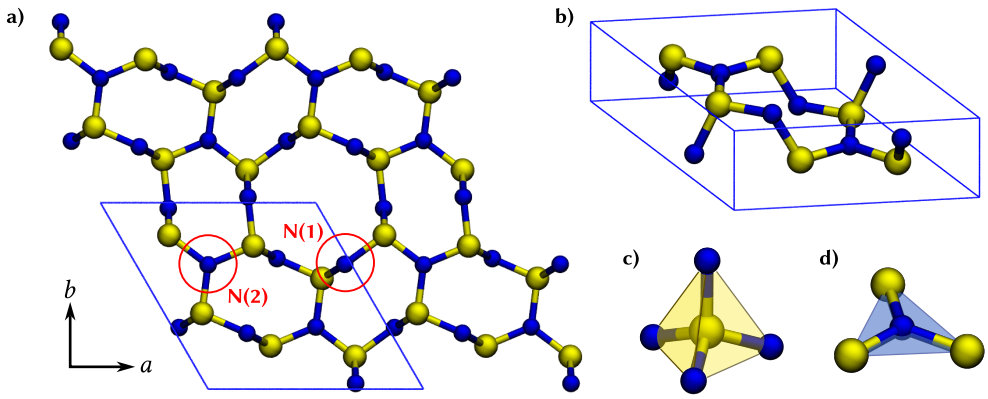

Figure 2.3: Structure of β-Si_3N_4: a) A $2 \times 2 \times 1$ supercell viewed along the c-axis showing the stack of eight- and twelve-membered rings forming a tube-like structure. The two distinct nitrogen sites N(1) and N(2) are highlighted. b) Illustration of the hexagonal unit cell with two formula units of Si_3N_4. c) The tetrahedral coordination environment of Si. d) The trigonal-planar coordination environment of N.

formula units per unit cell. The structure features one symmetrically unique silicon atom and two symmetrically distinct nitrogen atoms, denoted N(1) and N(2), see Figure 2.3a and b.[16,17] The Si atoms are tetrahedrally coordinated by four N atoms, while all N atoms are threefold coordinated by Si forming an equilateral triangle (Figure 2.3c and d). In less systematic terms, the structure can be described as vertically interlinked layers in the *ab*-plane with eight- and twelve-membered rings forming tubes along the *c*-direction. The coordination polygon of N(2) lays horizontally in the *ab*-plane embedded into three eight-membered rings. In contrast, N(1) is part of the twelve-membered rings, with its equilateral triangle being parallel to the *c*-axis.

2.2 Classical Interatomic Potentials

In general, interatomic potentials describe the interactions between atoms, which govern the physical and chemical properties of a material.[18,19] An accurate description of these interactions not only explains experimental observations but also enables predictive modeling of material behavior.[20–23] The underlying physics of an atomistic system is governed by quantum mechanics, which generally does not allow to obtain exact solutions for anything containing more than a single electron. For sake of simplicity, it is convenient to bypass the

quantum mechanical solution and simply express the interaction between atoms by analytical functions, which are motivated by chemical intuition. The earliest attempts to do so date back to the 1920s,[24–30] when such potentials were developed based on classical mechanics – hence the term *classical potentials*. Under the assumption that the interatomic potential V is solely dependent on the positions of the nuclei $\boldsymbol{r} = (\boldsymbol{r}_1, \boldsymbol{r}_2, ..., \boldsymbol{r}_N)$ and that the individual physical contributions, *e.g.,* Coulombic or dispersion[31] interactions, are additive, the total potential can be expressed as an expansion of many-body terms reading[32]

$$V(\boldsymbol{r}) = \sum_{i}^{N} V_1(\boldsymbol{r}_i) + \sum_{i}^{N}\sum_{j>i}^{N} V_2(\boldsymbol{r}_i \boldsymbol{r}_j) + \sum_{i}^{N}\sum_{j>i}^{N}\sum_{k>j}^{N} V_3(\boldsymbol{r}_i \boldsymbol{r}_j \boldsymbol{r}_k) + ... \quad . \tag{2.10}$$

The resulting forces $\boldsymbol{F}_i$ on atom i is given by the negative gradient of the potential

$$\boldsymbol{F}_i(\boldsymbol{r}_i) = -\frac{\partial V(\boldsymbol{r})}{\partial \boldsymbol{r}_i} \tag{2.11}$$

The potentials used in this thesis to model amorphous solids (see Section 3.1) encompass only two- and three-body terms with a varying degree of physical interpretability and numerical flexibility to match the experimental observations. The following sections provide a brief introduction to the standard force fields taken from literature.

2.2.1 The MG2 Potential

The MG2 potential has originally been developed by Marian *et al.*[33] to model Si–N–B ceramics. In comparison to other force fields developed for Si_3N_4,[34] it also yields excellent amorphous Si_3N_4 structures, especially concerning the defect concentration, which plays a pivotal role for the follow-up electronic structure calculations. Furthermore, the MG2 potential does not include charges and thus circumvents the problems associated with the long-ranged Coulombic interactions, *i.e.,* the self-interaction with periodic images, the non-zero potential when truncating at a finite distance, or costly Fourier transforms when applying techniques like Ewald summation.[35] The MG2 potential is based on the Morse potential[36] to describe the attraction between Si and N reading

$$V_{\mathrm{SiN}}(r) = D_{\mathrm{e}} \left[\left(1 - e^{a(r-r_0)}\right)^2 - 1 \right] \tag{2.12}$$

Table 2.1: The force field parameters of the MG2 potential.[33]

Elements	Type	Parameter	Unit	Value
Si–N	Morse	D_e	eV	3.88461
		a	$Å^{-1}$	2.32660
		r_0	Å	1.62136
Si–Si	general exponential	A	Å	177.510
		ρ	Å	0.636 85
N–N	general exponential	A	Å	2499.01
		ρ	Å	0.360 29
all	P_5 polynomial	x_i	Å	4.3
		x_o	Å	5.8

with the depth of the potential well D_e, the width of the well a, and the equilibrium distance r_0. The repulsion between homonuclear atoms is given by a simple, general exponential

$$V_{\mathrm{SiSi/NN}}(r) = \frac{A}{r} e^{-r/\rho} \tag{2.13}$$

with the empirical parameters A and ρ. Finally, a fifth-order polynomial

$$\begin{aligned} P_5(r) = (x_o - x_i)^{-5} \left[-6r^5 + 15\,(x_i + x_o)\, r^4 - 10\left(x_i^2 + 4x_i x_o + x_o^2\right) r^3 \right. \\ \left. +30\left(x_i^2 x_o + x_i x_o^2\right) r^2 - 30 x_i^2 x_o^2 r + 10 x_i^2 x_o^3 + x_o^5 - 5 x_i x_o^4 \right] \end{aligned} \tag{2.14}$$

is applied in the range $x_i < r < x_o$ as a global taper function to ensure a smooth convergence to zero. The resulting potential curves are displayed in Figure 2.4a and the force field parameters are listed in Table 2.1.

2.2.2 The BKS Potential

Due to its high commercial and academic relevance, there are plenty of classical potentials for SiO_2 available,[37–48] many of which with specific purposes like studying ion diffusion,[43,44] heat transport,[45] and phase transitions.[46–48] When it comes to generating amorphous structures for SiO_2, the BKS potential[49] is considered the "gold standard" as besides reproducing a wide range of physical properties with good accuracy, it generates an ideal continuous network of SiO_4-tetrahedra (compare Section 3.1). For this reason, the BKS potential is used at large as the reference and to generate training data in Chapter 4.

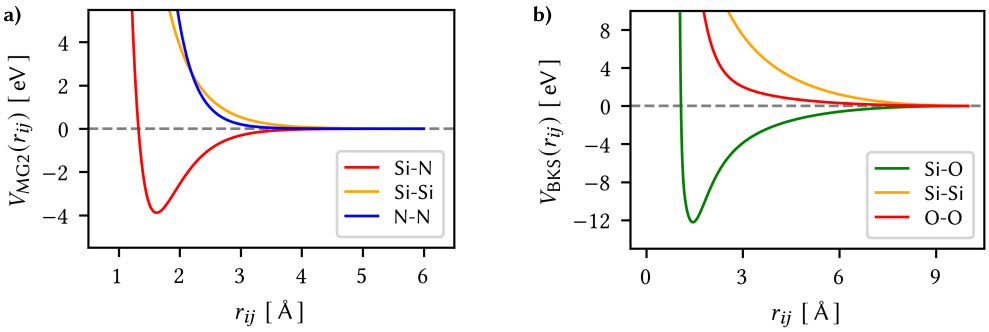

Figure 2.4: The pair potential curves of a) the MG2 potential[33] for Si_3N_4 and b) the BKS potential[49] with the SHIK-1[50,51] parameterization for SiO_2.

The BKS potential shown in Figure 2.4b is comprised of a short-ranged Buckingham potential (V_{buck}),[52] a Coulomb term (V_{coul}),[53] and a taper function (f_{taper}), such that

$$V_{\text{BKS}}(r_{ij}) = f_{\text{taper}}(r_{ij}) \left[V_{\text{buck}}(r_{ij}) + V_{\text{coul}}(r_{ij}) \right] \quad . \tag{2.15}$$

Here, V_{buck} has been extended by a short-range repulsion term by Sundararaman *et al.*[50,51] to prevent it from catastrophic divergence to $-\infty$ at short interatomic distances. That makes

$$V_{\text{buck}}(r_{ij}) = A \exp\left(-B r_{ij}\right) - \frac{C}{r_{ij}^6} + \frac{D}{r_{ij}^{24}} \quad . \tag{2.16}$$

The Coulomb term, while simple on paper, poses a serious challenge since it does not converge rapid enough to zero for the length scales typically encountered in atomistic simulations. A premature, hard cut-off leads to a not-negligible discontinuity in the potential. Therefore, the Wolf truncation method[54,55] is used, that tapers the Coulomb term at the cut-off distance r_{cut} according to

$$V_{\text{coul}}(r_{ij}) = \frac{q_i q_j}{4\pi\varepsilon_0} \left[\frac{1}{r_{ij}} - \frac{1}{r_{\text{cut}}} + \frac{r_{ij} - r_{\text{cut}}}{r_{\text{cut}}^2} \right] \tag{2.17}$$

with the vacuum permittivity ε_0. Lastly, the f_{taper} ensures smooth convergence to zero at r_{cut} via

$$f_{\text{taper}}(r_{ij}) = \exp\left(-\frac{\gamma^2}{\left(r_{ij} - r_{\text{cut}}\right)^2} \right) \quad . \tag{2.18}$$

Table 2.2: The force field parameters of the BKS potential[49] with the SHIK-1 parameterization.[50] potential. Global parameters are $q_{\mathrm{Si}} = -2q_{\mathrm{O}} = 1.7755\,e$, $r_{\mathrm{cut}} = 10\,\text{Å}$, and $\gamma = 0.2\,\text{Å}$.

Elements	A [eV]	B [Å^{-1}]	C [eVÅ^{6}]	D [eVÅ^{24}]
Si–Si	2797.9	4.407	0.0	3 423 204
Si–O	23 107.8	5.098	139.7	66
O–O	1120.5	2.893	26.1	16 800

The BKS potential has been (re-)parameterized more than once, mostly to adjust it to specific use-cases or to diminish numerical instabilities. In this thesis, the SHIK-1[50] parameterization is used as benchmarks have shown that among the screened force fields it is the most robust for generating amorphous structures. The parameters are provided in Table 2.2.

2.2.3 The Tersoff Potential

The Tersoff potential is classified as a *bond-order potential*, including an analytical term that captures the local environment of the reference atom.[56] Simple pair potentials are generally not capable of capturing deviations in bond angles, vacant binding sites, or additional binding partners as the energies depend solely on pairwise interactions. To address this, bond-order potentials include a term depending on the bond angle between triplets of particles and penalizes deviations from the equilibrium angle. By doing so, the correct coordination environment is preserved as any coordination polyhedron has a characteristic bond angle, *e.g.,* 109.47° for the tetrahedron. A critical disadvantage of three-body potentials, compared to the pair potentials, is their less favorable computational scaling due to the considerably larger neighbor lists. The Tersoff potential mitigates this issue by employing short cut-off radii, *i.e.,* by accounting only for interactions within the first coordination shell (see Figure 2.5). This approach is an acceptable compromise when atomic diffusivity is low. However, it can introduce significant artifacts when atoms move across the cut-off region, as the steep taper function generates artificially large forces near the boundary.

The Tersoff potential is commonly implemented by splitting the pair potential V_{ij} into a repulsive term V_{R} and an attractive term V_{A} according to

$$V_{ij}(r_{ij}) = f_{\mathrm{c}}(r_{ij}) \left[V_{\mathrm{R}}(r_{ij}) - b_{ij} V_{\mathrm{A}}(r_{ij}) \right] , \tag{2.19}$$

where r_{ij} is the pair distance between the atoms i and j. The two-body terms V_R and V_A are expressed using general exponentials

$$V_\mathrm{R}(r_{ij}) = A \exp\left(-\lambda_1 r_{ij}\right) \tag{2.20}$$

$$V_\mathrm{A}(r_{ij}) = B \exp\left(-\lambda_2 r_{ij}\right) \tag{2.21}$$

that rely on the four parameters A, B, λ_1 and λ_2. Importantly, the bond-order term $b_{ij} \in [0, 1]$ modulates V_A so that deviations from the equilibrium bond angle $\theta_{0,ijk}$ lead to an energetic penalty. b_{ij} reads

$$b_{ij} = \left(1 + \beta_i^{n_i} \zeta_{ij}^{n_i}\right)^{-1/2n_i} \tag{2.22}$$

$$\zeta_{ij} = \sum_{k \neq i,j} f_\mathrm{c}(r_{ik}) g(\theta_{ijk}) \tag{2.23}$$

$$g(\theta_{ijk}) = 1 + \frac{c_i^2}{d_i^2} - \frac{c_i^2}{d^2 + \left[h_i - \cos(\theta_{ijk})\right]^2} \,. \tag{2.24}$$

where θ_{ijk} is the bond angle centered on atom i and with its neighbors j, and k. h is the cosine of the equilibrium bond angle $\cos(\theta_{0,ijk})$. Lastly, the taper function (f_c) is constructed in such a way that the potential goes to zero in the range between R_1 and R_2. The cut-off range is set such that the potential encompasses only the neighbors in the first coordination shell, which is passable for simulations of crystalline solids at room temperature, but becomes difficult for the amorphous phase where the long tail in the radial distribution function can

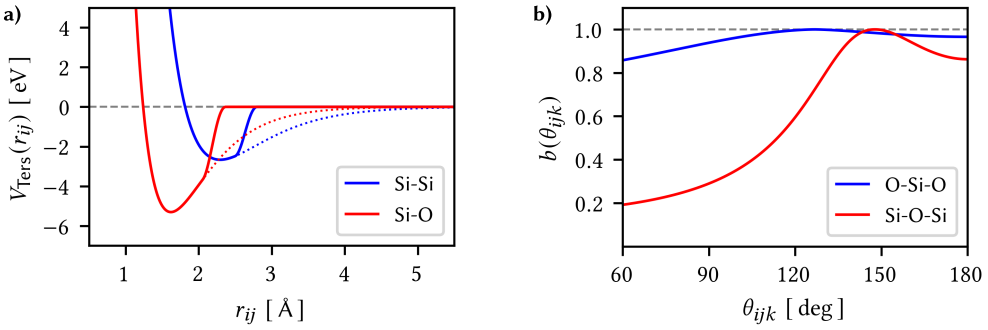

Figure 2.5: a) The pair potentials V_{ij} as a function of the pair distance r_{ij} for $b_{ij} = 1$ without (dotted) and with the taper function applied (solid) and b) the bond order function b depending on the bond angle θ_{ijk} of the Tersoff force field[56] according to the Munetoh parameterization.[57]

Table 2.3: The force field parameters by Munetoh *et al.*[57] for the Tersoff potential[56] designed to model various SiO_2 polymorphs including the amorphous.

		Two-body terms		
Parameter	Unit	Si–Si	Si–O	O–O
A	eV	1.8308×10^{3}	1.8565×10^{3}	$1.882\,55\times10^{3}$
B	eV	4.7118×10^{2}	3.7869×10^{2}	$2.287\,87\times10^{2}$
λ_1	$Å^{-1}$	2.4799	3.3255	4.171 08
λ_2	$Å^{-1}$	1.7322	2.0446	2.356 92
R_1	Å	2.5	2.06	1.7
R_2	Å	2.8	2.37	2.0
		Three-body terms		
Parameter		X–Si–X		X–O–X
c		1.0039×10^{5}		$6.469\,21\times10^{4}$
d		1.6217×10^{1}		4.111 27
h		$-0.598\,25$		$-8.459\,22\times10^{-1}$
n		7.8734×10^{-1}		1.049 68
β		1.1×10^{-6}		1.1632×10^{-7}

overlap with the aggressive f_c between R_1 and R_2. The taper reads

$$f_c(r_{ij}) = \begin{cases} 1 & \text{if } r_{ij} < R_1, \\ \frac{1}{2} + \frac{1}{2}\cos\left(\pi \frac{r_{ij}-R_1}{R_2-R_1}\right) & \text{if } R_1 \leq r_{ij} \leq R_2, \\ 0 & \text{if } r_{ij} > R_2 \end{cases} . \tag{2.25}$$

In the context of this thesis, the Tersoff potential is used in Chapter 4 as concrete example on how Bayesian optimization can help at finding the best force field parameters (within a given functional for reproducing particular properties) and how to better understand the black-box nature of complex, N-dimensional optimization problems.

2.3 Density Functional Theory

As indicated in the previous section, a quantum mechanical description is essential for accurately modeling atomistic systems, as it captures the wave-like nature of electrons and their interactions, which cannot be represented within a classical framework. In quantum mechanics, the electronic state of a system is represented by the wave function $\Psi(\boldsymbol{r})$, from which the total energy can, in principle, be obtained through the electronic Schrödinger equation[58] within the Born-Oppenheimer approximation.[59] It is well known that an analytical solution to the Schrödinger equation is not available for systems containing two or more electrons. Consequently, approximations must be introduced, and the many body problem arising from the large number of interacting nuclei and electrons in a chemical system generally remains unsolved. In order to circumvent both the explicit solution of the Schrödinger equation and the associated many body problem, Thomas[60] and Fermi[61] proposed in 1927 that the total energy of a system could instead be expressed as a functional of the electron density. The electron density for a system with n electrons can be obtained from the many electron wave function $\phi(\boldsymbol{r}_1, \boldsymbol{r}_2, ..., \boldsymbol{r}_N)$ *via*

$$\rho(\boldsymbol{r}) = N \int \phi^*(\boldsymbol{r}, \boldsymbol{r}_2, ..., \boldsymbol{r}_N)\phi(\boldsymbol{r}, \boldsymbol{r}_2, ..., \boldsymbol{r}_N)\ \mathrm{d}\boldsymbol{r}_2 ... \mathrm{d}\boldsymbol{r}_N \tag{2.26}$$

with the normalization condition

$$N = \int \rho(\boldsymbol{r})\ \mathrm{d}\boldsymbol{r}\ . \tag{2.27}$$

However, it was not until 1964 that Hohenberg and Kohn[62] provided the formal foundation for such an approach by proving a theorem stating (i) the ground state properties of a system are uniquely determined by its electron density, and (ii) there exists a universal energy functional of the density whose minimization yields the exact ground state energy and density. This allows the total energy to be expressed as the sum of the kinetic energy T, the electron-electron repulsion V_{ee}, and the electron-nucleus attraction V_{ne}

$$E[\rho] = T[\rho] + V_{\mathrm{ee}}[\rho] + V_{\mathrm{ne}}[\rho] \tag{2.28}$$

$$= \int \rho(\boldsymbol{r}) v_{\mathrm{ext}}(\boldsymbol{r})\, \mathrm{d}\boldsymbol{r} + F_{\mathrm{HK}}[\rho]\ , \tag{2.29}$$

where $V_{\mathrm{ne}}[\rho]$ is written as an external potential $v_{\mathrm{ext}}(\boldsymbol{r})$, reading

$$v_{\mathrm{ext}}(\boldsymbol{r}) = \sum_i -\frac{Z_i}{|\boldsymbol{r} - \boldsymbol{R}_i|} \,. \tag{2.30}$$

While the Hohenberg-Kohn theorems established the theoretical foundation of density functional theory, they do not provide an explicit form of the universal functional $F_{\mathrm{HK}}[\rho]$. To make the approach practically applicable, it is necessary to reformulate the problem in a way that allows the ground-state density and energy to be computed efficiently.

2.3.1 The Kohn-Sham Method

In the formalism introduced thus far, the universal functional $F[\rho]$ comprises the electronic kinetic energy $T[\rho]$ and the electron-electron interaction energy $V_{\mathrm{ee}}[\rho]$. In particular, the kinetic energy of the many-body system is difficult to approximate in practice. A decisive breakthrough was achieved by Kohn and Sham,[63] who reformulated the problem in terms of a fictitious system of non-interacting electrons that yields the same ground-state density as the real, interacting system. In this framework, the universal functional is decomposed to

$$F[\rho] = T_s[\rho] + J[\rho] + E_{\mathrm{xc}}[\rho] \,, \tag{2.31}$$

where $T_s[\rho]$ is the kinetic energy of the non-interacting reference system, $J[\rho]$ is the classical Coulomb (Hartree) energy describing the electron-electron repulsion, and $E_{\mathrm{xc}}[\rho]$ accounts for all remaining quantum-mechanical effects, including exchange and correlation as well as the difference between $T[\rho]$ and $T_s[\rho]$

$$E_{\mathrm{xc}} = (T[\rho] - T_s[\rho]) + (V_{\mathrm{ee}}[\rho] - J[\rho]) \,. \tag{2.32}$$

The Hartree energy can be expressed explicitly as a functional of the electron density

$$J[\rho] = \frac{1}{2} \iint \frac{\rho(\boldsymbol{r})\rho(\boldsymbol{r}')}{|\boldsymbol{r} - \boldsymbol{r}'|} \, \mathrm{d}\boldsymbol{r} \, \mathrm{d}\boldsymbol{r}' \,. \tag{2.33}$$

However, no analogous expression exists for the kinetic energy. To evaluate $T_s[\rho]$, the Kohn-Sham approach reintroduces single-particle orbitals $\chi_i(\boldsymbol{r})$, which yield the electron density

$$\rho(\boldsymbol{r}) = \sum_i |\chi_i(\boldsymbol{r})|^2 \,. \tag{2.34}$$

The kinetic energy with these orbitals are explicitly given by

$$T_s[\rho] = \sum_i^N \langle \chi_i | -\frac{1}{2}\nabla^2 | \chi_i \rangle \tag{2.35}$$

Application of the second part of the Hohenberg-Kohn theorem leads to a set of single-particle equations for the non-interacting system, which is given by

$$\hat{h}_s \chi_i(\boldsymbol{r}) = \left[-\frac{1}{2}\nabla^2 + v_s(\boldsymbol{r}) \right] \chi_i(\boldsymbol{r}) = \epsilon_i \chi_i(\boldsymbol{r}) \,, \tag{2.36}$$

where $v_s(\boldsymbol{r})$ is the effective potential that yields the target ground-state density. It includes the external potential v_{ext}, the Hartree potential v_{H} to account for the other electrons, and the exchange-correlation potential v_{xc}

$$v_s(\boldsymbol{r}) = v_{\text{ext}}(\boldsymbol{r}) + v_{\text{H}}(\boldsymbol{r}) + v_{\text{xc}}(\boldsymbol{r}) = v_{\text{ext}}(\boldsymbol{r}) + \int \frac{\rho(\boldsymbol{r}')}{|\boldsymbol{r} - \boldsymbol{r}'|} \, \mathrm{d}\boldsymbol{r}' + \frac{\delta E_{\text{xc}}[\rho]}{\delta \rho(\boldsymbol{r})} \tag{2.37}$$

In this formalism, the exchange-correlation functional is the only remaining unknown contribution. Unfortunately, an exact expression for this functional, derived entirely from first principles, has not yet been found. Consequently, one must rely on approximate forms of $E_{\text{xc}}[\rho]$, the most relevant of which will be discussed in the following section.

2.3.2 Exchange-Correlation Functionals

The simplest approximation for the exchange-correlation functional assumes that $\rho(\boldsymbol{r})$ varies only slowly in space, so that the system can locally be regarded as a homogeneous electron gas (HEG). In this case, E_{xc} depends only on the local value of the density, which leads to the *Local Density Approximation* (LDA). The exchange-correlation energy is then expressed as

$$E_{\text{xc}}^{\text{LDA}}[\rho] = \int \rho(\boldsymbol{r}) \varepsilon_{\text{xc}}^{\text{HEG}}(\rho(\boldsymbol{r})) \, \mathrm{d}\boldsymbol{r} \,, \tag{2.38}$$

where $\varepsilon_{\mathrm{xc}}^{\mathrm{HEG}}$ denotes the exchange-correlation potential of the homogeneous electron gas at density ρ. $\varepsilon_{\mathrm{xc}}^{\mathrm{HEG}}$ is further divided into exchange and correlation contributions,

$$\varepsilon_{\mathrm{xc}}^{\mathrm{HEG}}(\rho) = \varepsilon_{\mathrm{x}}^{\mathrm{HEG}}(\rho) + \varepsilon_{\mathrm{c}}^{\mathrm{HEG}}(\rho) \,. \tag{2.39}$$

From the early work of Thomas,[60] Fermi,[61] and Dirac,[64] an explicit analytical expression is known for the exchange energy

$$\varepsilon_{\mathrm{x}}^{\mathrm{HEG}}(\rho) = -\frac{3}{4}\left(\frac{3}{\pi}\right)^{1/3}\rho^{1/3} \,, \tag{2.40}$$

whereas no such closed-form expression exists for the correlation energy. Instead $\varepsilon_{\mathrm{c}}^{\mathrm{HEG}}(\rho)$, has been obtained from quantum Monte-Carlo calculations for the homogeneous electron gas[65] and implemented through empirically parameterized forms, such as those proposed by Perdew-Zunger,[66] Perdew-Wang,[67,68] and Vosko, Wilk, and Nusair.[69] Despite its simplicity, the LDA performs remarkably well for metallic systems, where the assumption of a nearly uniform electron density is reasonably well justified. However, for most other chemical systems – particularly molecules – this approximation breaks down, as real electron densities exhibit significant spatial inhomogeneities.

That is why the *Generalized Gradient Approximation* (GGA) was introduced, extending the LDA by explicitly incorporating information about the local density gradient. Formally, E_{xc} reads

$$E_{\mathrm{xc}}^{\mathrm{GGA}}[\rho] = \int \rho(\boldsymbol{r})\varepsilon_{\mathrm{xc}}^{\mathrm{GGA}}(\rho(\boldsymbol{r}), \nabla\rho(\boldsymbol{r}))\,\mathrm{d}\boldsymbol{r} \,, \tag{2.41}$$

where $\varepsilon_{\mathrm{xc}}^{\mathrm{GGA}}$ typically comes in the form of

$$\varepsilon_{\mathrm{xc}}^{\mathrm{GGA}} = \varepsilon_{\mathrm{xc}}^{\mathrm{LDA}}(\rho) + \Delta\varepsilon_{\mathrm{xc}}\left[\frac{|\nabla\rho(\boldsymbol{r})|}{\rho^{4/3}(\boldsymbol{r})}\right] \,. \tag{2.42}$$

Similar to the LDA functionals, there is no universal expression for $\varepsilon_{\mathrm{xc}}^{\mathrm{GGA}}$ and numerous GGA functionals have been developed with varying degrees of empiricism, often balancing universality versus specialization for particular applications. Nevertheless, GGAs represent a significant improvement over LDA, providing reasonably accurate atomization energies, reaction barriers, and molecular structures across a wide range of chemical systems.

The workhorse functional employed in this thesis is the non-empirical GGA developed by Perdew, Burke, and Ernzerhof (PBE).[70,71] The PBE exchange energy is written as

$$E_{\mathrm{x}}^{\mathrm{PBE}}[\rho(\boldsymbol{r}), \nabla\rho(\boldsymbol{r})] = \int \rho\varepsilon_{\mathrm{x}}^{\mathrm{HEG}}(\boldsymbol{r})F(s)\ \mathrm{d}\boldsymbol{r}\ , \tag{2.43}$$

with the enhancement factor $F^{\mathrm{PBE}}(s)$

$$F^{\mathrm{PBE}}(s) = 1 + \kappa\left(1 - \frac{1}{1 + \mu s^2/\kappa}\right) \tag{2.44}$$

where the dimensionless reduced gradient s is

$$s = \frac{|\nabla\rho(\boldsymbol{r})|}{2(3\pi^2)^{1/3}\rho^{4/3}(\boldsymbol{r})}\ . \tag{2.45}$$

The correlation energy is expressed as

$$E_{\mathrm{c}}^{\mathrm{GGA}}[\rho(\boldsymbol{r}), \nabla\rho(\boldsymbol{r})] = \int \rho(\boldsymbol{r})\left[\varepsilon_{\mathrm{c}}^{\mathrm{HEG}} + H(\rho(\boldsymbol{r}), \nabla\rho(\boldsymbol{r}))\right]\mathrm{d}\boldsymbol{r} \tag{2.46}$$

with the gradient contribution H being defined as

$$H(\rho(\boldsymbol{r}), \nabla\rho(\boldsymbol{r})) = \gamma \ln\left[1 + \frac{\beta\gamma}{t^2}\right] \tag{2.47}$$

with the reduced gradient $t = |\nabla\rho|/2k_s\rho$ and the Thomas-Fermi screening wave number k_s. The parameters $\mu = 0.219\,51$, $\kappa = 0.804$, $\beta = 0.066\,725$, $\gamma = 0.031\,091$ are all derived from exact physical constraints rather than empirical fitting, ensuring that PBE satisfies known limits for both slowly varying densities and high-density homogeneous electron gases.

Altogether, GGA functionals have proven robust for most chemical systems,[72–74] though a number of problematic cases persist. Unlike in Hartree-Fock theory, electron self-interaction is not completely canceled in GGA exchange, which can lead to spin contamination in open-shell systems and makes anions particularly challenging to treat accurately. In the case of PBE, the functional tends to produce overly delocalized ground-state electron densities, resulting in a systematic underestimation of band gaps.[75,76] This limitation is especially problematic for semiconductors and defect states, as mid-gap levels are often poorly described.[77,78]

To address these shortcomings, a fraction of exact Hartree-Fock (HF) exchange can be incorporated, giving rise to so-called *hybrid functionals*.[79,80] In the simplest formulation, this is achieved by mixing a fixed fraction of HF exchange into a GGA exchange-correlation functional. The PBE0 functional[81] is one such example, combining 25 % exact HF exchange with 75 % PBE exchange while retaining the full PBE correlation contribution, thus

$$E_{\mathrm{xc}}^{\mathrm{PBE0}} = aE_{\mathrm{x}}^{\mathrm{HF}} + (1-a)E_{\mathrm{x}}^{\mathrm{PBE}} + E_{\mathrm{c}}^{\mathrm{PBE}} \,, \tag{2.48}$$

with the mixing coefficient $a = 1/4$. While conceptually straight-forward, the evaluation of the two-electron integrals in the HF calculation scales as $\mathcal{O}(N^4)$ with N being the number of electrons, rendering hybrid functionals computationally expensive for large systems. In insulators and semiconductors, however, the exchange interaction decays exponentially with distance. Exploiting this property, Heyd, Scuseria, and Ernzerhof proposed a screened hybrid functional,[82,83] which applies a screened Coulomb potential to split the electron-electron interaction into short- and long-range components:[84,85]

$$\frac{1}{r} = \frac{\mathrm{erfc}(\omega r)}{r} + \frac{\mathrm{erf}(\omega r)}{r} \,. \tag{2.49}$$

By neglecting the long-range Hartree-Fock contribution, the resulting screened hybrid functional is defined as

$$E_{\mathrm{xc}}^{\mathrm{HSE}} = aE_{\mathrm{x}}^{\mathrm{HF,SR}}(\omega) + (1-a)E_{\mathrm{x}}^{\mathrm{PBE,SR}}(\omega) + E_{\mathrm{x}}^{\mathrm{PBE,LR}}(\omega) + E_{\mathrm{c}}^{\mathrm{PBE}} \tag{2.50}$$

where $\omega = 0.11\,\mathrm{Bohr}^{-1}$ is the range-separation parameter.[86] The HSE functional significantly improves the description of solids, particularly the band gaps of insulators and semiconductors.[85] For this reason, the HSE06 version is employed in this thesis to study charge-trapping phenomena in a-Si_3N_4.

2.4 The Gaussian Plane Wave Method

2.4.1 Localized Basis Sets

Up to this point, DFT has been discussed under the implicit assumption that the electron density can be conveniently constructed. Although $\rho(\boldsymbol{r})$ is, in principle, a simple three-dimensional scalar field, the introduction of single-particle orbitals in the non-interacting Kohn-Sham reference system[63] requires careful implementation in practice. While Kohn-Sham orbitals do strictly speaking not have a physical meaning, they nonetheless provide valuable semi-quantitative insights into the relative energy levels, spatial distribution, and symmetry of electronic states.[87] This motivates expressing $\rho(\boldsymbol{r})$ in terms of atomic wavefunction-like basis functions $\varphi(r)$. In such basis, the electron density given as

$$\rho(\boldsymbol{r}) = \sum_{i}^{n} \varphi_i^*(\boldsymbol{r})\varphi_i(\boldsymbol{r}) \,. \tag{2.51}$$

A natural choice for φ are hydrogen-like orbitals, which have an analytical form

$$\varphi_{\zeta,n,l,m}(r,\theta,\vartheta) = NY_{l,m}(\theta,\vartheta)r^{n-1}\exp\left(-\zeta r\right) \,. \tag{2.52}$$

N is the normalization constant, $Y_{l,m}(\theta,\vartheta)$ are spherical harmonics describing the angular part, and the exponential term represents the radial decay. These so-called *Slater-type orbitals* (STOs) accurately capture the near-nucleus cusp and the correct exponential decay at large distances. However, they are computationally demanding: They lack simple analytic expressions for many-center integrals, and their radial form is not smooth at $r = 0$. To overcome these difficulties, *Gaussian-type orbitals* (GTOs) were introduced,[88–90] defined as

$$\varphi_{\zeta,n,l,m}(r,\theta,\vartheta) = NY_{l,m}(\theta,\vartheta)r^{2n-2-1}\exp\left(-\zeta r^2\right) \,. \tag{2.53}$$

The Gaussian exponent ensures analytic integrability, making GTOs computationally much more efficient. However, individual Gaussians do not reproduce the nuclear cusp correctly and decay too rapidly at large r. In practice, these deficiencies are mitigated by using so-called contracted Gaussian functions, which are linear combinations of primitive GTOs de-

signed to mimic the shape of STOs:

$$\phi^{\text{STO-nG}} = \sum_{j}^{n} c_j \varphi_{\zeta,j} \tag{2.54}$$

where n denotes the number of primitive Gaussians. This approach was first proposed by Hehre *et al.*[91] in the STO-nG family of basis sets. Despite their simplicity, STO-nG basis sets provide reasonable accuracy for small molecules composed of light elements. Modern electronic-structure calculations, however, employ more flexible and systematically improvable schemes — such as double-ζ or triple-ζ expansions, split-valence basis sets that treat valence and core orbitals differently,[92–94] and polarization or diffuse functions that enhance angular flexibility and describe electronic tails.[95–98]

2.4.2 Plane Waves

As introduced earlier, perfectly crystalline solids are periodic in all three spatial directions. This provides a convenient ansatz for the wave-functions. According to Bloch's theorem,[99] the eigenfunctions of a periodic potential can be written as

$$\phi_{\boldsymbol{k}}(\boldsymbol{r}) = u_{\boldsymbol{k}}(\boldsymbol{r}) e^{i\boldsymbol{k}\boldsymbol{r}} \tag{2.55}$$

where $u_{\boldsymbol{k}}(\boldsymbol{r})$ is a lattice-periodic function satisfying $u_{\boldsymbol{k}}(\boldsymbol{r}) = u_{\boldsymbol{k}}(\boldsymbol{r} + \boldsymbol{R})$. The periodic part $u_{\boldsymbol{k}}(\boldsymbol{r})$ can itself be expanded as a Fourier series of reciprocal lattice vectors $\boldsymbol{G}$ introduced in Section 2.1.2 such that

$$u_{\boldsymbol{k}}(\boldsymbol{r}) = \sum_{\boldsymbol{G}} c_{\boldsymbol{k}+\boldsymbol{G}} e^{i\boldsymbol{G}\boldsymbol{r}} \tag{2.56}$$

so that the full Bloch wavefunctions becomes

$$\phi_{\boldsymbol{k}}(\boldsymbol{r}) = \sum_{\boldsymbol{G}} c_{\boldsymbol{k}+\boldsymbol{G}} e^{i(\boldsymbol{k}+\boldsymbol{G})\boldsymbol{r}} \ . \tag{2.57}$$

In this context, the wave vector $\boldsymbol{k}$ is referred to as the Bloch vector. It serves as a quantum number labeling the eigenstates of the periodic Hamiltonian and lies within the first Brillouin zone of the reciprocal lattice. Physically, wave vectors that differ by a reciprocal lattice vector $\boldsymbol{G}$ describe the same crystal momentum and therefore represent equivalent electronic

states. For a finite crystal or a numerical calculation, the continuous set of $\boldsymbol{k}$-vectors is sampled on a discrete mesh to approximate integrals over the Brillouin zone. Each k-point, combined with the set of reciprocal lattice vectors $\boldsymbol{G}$, defines a complete plane-wave basis for expanding the electronic states corresponding to different bands with the same Bloch wave vector.

In practice, the infinite sum given by Equation 2.57 over reciprocal lattice vectors must be truncated to a finite number of plane waves. This is typically done by imposing a kinetic energy cutoff, such that only plane waves satisfying

$$\frac{\hbar^2}{2m_\mathrm{e}} |\boldsymbol{k} + \boldsymbol{G}|^2 \leq E_\mathrm{cut} \tag{2.58}$$

are included. The energy cutoff controls the completeness of the basis set: Higher cutoffs yield more accurate results at the cost of increased computational effort. Plane-wave bases offer several advantages, including systematic convergence, absence of basis-set superposition errors, and efficient evaluation of derivatives via fast Fourier transforms.

However, because plane waves are delocalized, describing the rapid oscillations of core electrons near nuclei would require prohibitively high cutoffs. This limitation is addressed by using pseudopotentials (see Section 2.4.4), which smooth the potential in the core region while retaining the correct description of the valence electrons.[100–102]

2.4.3 Gaussian Plane Waves

So far, two types of basis sets have been introduced: the localized GTOs and the fully delocalized plane waves. Local GTOs offer a conceptually straightforward approach to approximating atomic and molecular orbitals and are relatively easy to evaluate. However, they are inherently non-periodic, making Fourier-space operations inefficient. Moreover, the basis cannot be systematically converged by simply increasing the number of functions, and basis set superposition errors arise due to the interactions with an effectively infinite number of neighbors in a crystal. Plane waves, on the other hand, elegantly solve these issues, providing systematic convergence and computational efficiency. They do, however, have their own disadvantages: A large number of plane waves is required to describe rapid oscillations in the electronic density near the nuclei. Pseudopotentials alleviate this problem for core

electrons, but it can remain significant for heavier elements or for highly localized states, such as Anderson states that can appear at lattice defects.[103]

To combine the advantages of both approaches, the Gaussian and Plane Wave (GPW) approach has been developed.[104,105] It retains the locality of Gaussian functions for a compact representation of the Kohn-Sham orbitals while leveraging the periodicity and Fourier-space efficiency of plane waves for the electron density. In this hybrid framework, the Kohn-Sham orbitals are expanded in localized Gaussians, whereas the electron density is represented on an auxiliary plane-wave grid. This mixed representation enables an efficient evaluation of the Coulomb and exchange-correlation contributions while keeping the number of basis functions relatively small and preserving systematic convergence properties.

The Kohn-Sham GPW energy in the GPW formalism can be written as

$$E_{\mathrm{KS}}^{\mathrm{GPW}}[\rho] = T[\rho] + E_{\mathrm{xc}}[\tilde{\rho}] + E_{\mathrm{H}}[\tilde{\rho}] + E_{\mathrm{PP}}[\rho] \tag{2.59}$$

where $T[\rho]$ is the kinetic energy, E_{xc} and E_{H} are the exchange-correlation and Hartree energies evaluated from the auxiliary plane-wave density $\tilde{\rho}$, and E_{PP} accounts for the pseudopotential contributions as further detailed in Section 2.4.4. The real-space electron density $\rho(\boldsymbol{r})$ is constructed from the Gaussian basis expansion as

$$\rho(\boldsymbol{r}) = \sum_{\mu\nu} P_{\mu\nu}\varphi_{\mu}(\boldsymbol{r})\varphi_{\nu}(\boldsymbol{r}) \tag{2.60}$$

where $P_{\mu\nu}$ is the density matrix and $\varphi_{\mu}(\boldsymbol{r})$ are the contracted Gaussians basis functions (see Equation 2.54). While $T[\rho]$ can be evaluated directly from in the Gaussian basis, E_{xc} and E_{H} are most efficiently computed in reciprocal space. To this end, the electron density is expanded in an auxiliary plane-wave basis according to

$$\tilde{\rho}(\boldsymbol{r}) = \frac{1}{V}\sum_{|\boldsymbol{G}|<E_{\mathrm{cut}}} \rho(\boldsymbol{G})e^{i\boldsymbol{G}\boldsymbol{r}} \,, \tag{2.61}$$

where $\rho(\boldsymbol{G})$ are the Fourier coefficients of the density and E_{cut} is the cutoff introduced in Equation 2.58. This expression simply represents the Fourier transform of the real-space electron density truncated to a finite number of plane waves. In this representation, the

KS-GPW energy can be expressed as

$$E_{\mathrm{KS}}^{\mathrm{GPW}}[\rho] = \sum_{\mu\nu} P_{\mu\nu} \langle \varphi_\mu(\boldsymbol{r}) | -\frac{1}{2}\nabla^2 | \varphi_\nu(\boldsymbol{r}) \rangle + \sum_{\mu\nu} P_{\mu\nu} \langle \varphi_\mu(\boldsymbol{r}) | V_{\mathrm{PP}}(\boldsymbol{r}, \boldsymbol{r}') | \varphi_\nu(\boldsymbol{r}') \rangle + 4\pi V \sum_{|\boldsymbol{G}|<E_{\mathrm{cut}}} \frac{\tilde{\rho}^*(\boldsymbol{G})\tilde{\rho}(\boldsymbol{G})}{\boldsymbol{G}^2} + \int \tilde{\rho}(\boldsymbol{r}) E_{\mathrm{xc}}[\tilde{\rho}]\, \mathrm{d}\boldsymbol{r} \tag{2.62}$$

where V_{PP} represents the pseudopotential operator, and the third term corresponds to the Hartree energy evaluated in reciprocal space with the complex conjugate of the density $\tilde{\rho}^*$.

Altogether, the GPW method provides a highly efficient compromise between localized and delocalized representations. It enables density-functional calculations on systems containing hundreds to thousands of atoms with moderate computational effort, though at the cost of a slight reduction of accuracy compared to pure plane waves due to the finite completeness of the Gaussian basis.

2.4.4 Pseudopotentials

As already discussed, pseudopotentials are essential for performing periodic electronic-structure calculations with tractable computational cost. In this work, the Goedecker-Teter-Hutter (GTH)[106,107] separable dual-space Gaussian pseudopotentials are employed.[108] These pseudopotentials are constructed from analytic functions that are straightforward to evaluate in both real and reciprocal space, making them particularly well suited for the GPW method.

The GTH pseudopotential consists of a local and a non-local part. The local part is defined as

$$V_{\mathrm{local}}(r) = -\frac{Z_{\mathrm{ion}}}{r}\mathrm{erf}\left(\frac{r}{\sqrt{2}r_{\mathrm{loc}}}\right) + \exp\left[-\frac{1}{2}\left(\frac{r}{r_{\mathrm{loc}}}\right)^2\right] \times \left[C_1 + C_2\left(\frac{r}{r_{\mathrm{loc}}}\right)^2 + C_3\left(\frac{r}{r_{\mathrm{loc}}}\right)^4 + C_4\left(\frac{r}{r_{\mathrm{loc}}}\right)^6\right] \tag{2.63}$$

where Z_{ion} is the ionic charge in accordance with the number of electrons frozen into a pseudo-ionic core for a given element and r_{loc} is a cutoff parameter defining the range of the local potential. The constants C_1, C_2, C_3, C_4 are empirically fitted element specific constants.

The non-local part is expressed in a separable form as

$$V_l(\boldsymbol{r}, \boldsymbol{r}') = \sum_{i=1}^{3} \sum_{j=1}^{3} \sum_{m=-l}^{l} Y_{l,m}(\hat{r}) p_i^l(r) h_{ij}^l p_j^l(r') Y_{l,m}(\hat{r}') \tag{2.64}$$

where l is the angular momentum quantum number, $Y_{l,m}$ are the spherical harmonics, and h_{ij}^l are the matrix elements describe the coupling between the radial projectors $p_i^l(r)$ according to

$$p_i^l(r) = \frac{\sqrt{2} r^{l+2(i-1)}}{r_l^{l+(4i-1)/2} \sqrt{\Gamma\left(l + \frac{4i-1}{2}\right)}} \exp\left(-\frac{r^2}{2r_l^2}\right) . \tag{2.65}$$

Since both the local and non-local components are composed of Gaussians multiplied by low-order polynomials, they preserve their analytical form upon Fourier transformation, ensuring efficient evaluation in reciprocal space. The full GTH pseudopotential is given by

$$V(\boldsymbol{r}, \boldsymbol{r}') = V_{\text{loc}}(r) \delta(\boldsymbol{r} - \boldsymbol{r}') + \sum_l V_l(\boldsymbol{r}, \boldsymbol{r}') , \tag{2.66}$$

whereby the l-summation excludes the local channel. Further implementation details and explicit reciprocal-space expressions can be found in Reference [107]. The analytic dual-space form of the GTH pseudopotentials, together with the GPW representation, forms the basis of the efficient Quickstep implementation in CP2K[109] used throughout this work.

2.5 Modeling Solids and Defects

2.5.1 Periodic Boundary Conditions

When modeling bulk solids, the boundaries of the simulation box take on special significance. Without further treatment, they form surfaces, edges, and corners, which behave chemically and physically fairly different from the bulk. This is resolved by applying *periodic boundary conditions* (PBC) at the boundaries of the simulation cell as illustrated in Figure 2.6, effectively removing surfaces and turning the system into an infinite solid. In practice, PBCs are implemented using the *minimum image convention* (MIC) according to which the pair distance Δr_{ij} between two atoms is selected between the reference atom i and

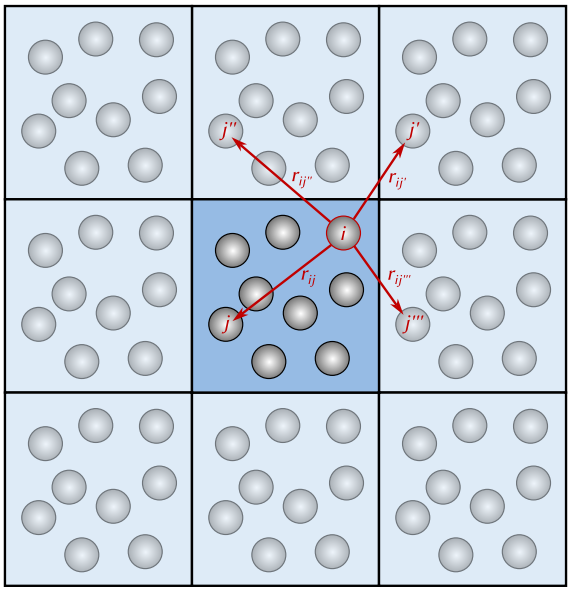

Figure 2.6: 2D-sketch of periodic boundary conditions: Images of the simulation box are placed around the original one, particles near the surface interact with the neighboring images. Pair distances according to the minimum image convention are calculated such that $\Delta r_{ij} = \min\{r_{ij}, r_{ij'}, r_{ij''}, r_{ij'''}\}$.

the closest image of j via

$$\Delta \boldsymbol{r}_{ij} = \boldsymbol{r}_i - \boldsymbol{r}_j - \boldsymbol{n}\boldsymbol{R} \tag{2.67}$$

with $\boldsymbol{R}$ being the translation vector of the crystal lattice as defined in Equation 2.2 and $\boldsymbol{n} \in \mathbb{Z}^3$ is chosen to minimize $\|\Delta \boldsymbol{r}_{ij}\|$.

When modeling solids using density functional theory (DFT), several technical aspects must be carefully considered to ensure reliable results. In general, DFT calculations are limited to a few hundred up to roughly a thousand atoms. This limitation becomes even more severe for hybrid functionals, since evaluating the two-electron integrals in the Hartree-Fock exchange term scales with $\mathcal{O}(N^4)$. Such system sizes can be sufficient to model nanoparticles, but they are far too small to capture the characteristic behavior of real, *e.g.,* not-perfectly crystalline, bulk solids. In principle, PBCs enable the simulation of an infinite crystal using only its smallest repeating unit. For a perfect, defect-free system, this representation is exact, provided that the Brillouin zone is sampled with sufficient k-point density. In such cases, PBCs correctly reproduce both the long- and short-range periodic response of the infinite solid.

In practice, however, finite-size effects arise when the simulation cell is not sufficiently large. Incomplete Brillouin-zone sampling can cause artificial discretization of the electronic states, particularly in small cells or disordered systems where Γ-point sampling is commonly employed. Numerical factors such as limited plane-wave cutoffs or coarse real-space grids can further prevent full convergence of the electronic density, compounding these finite-size artifacts. In addition, localized perturbations, such as point defects or charge localization, may interact with their own periodic images through long-range electrostatic or strain fields, leading to spurious self-interaction errors in the total energy.

Moreover, certain physical observables inherently require larger simulation domains to be faithfully represented. For example, diffusion simulations must extend beyond the ballistic regime, and phonon-related phenomena, such as heat transport, demand cell sizes that encompass long-wavelength vibrational modes. These finite-size effects can be systematically reduced by constructing extended supercells, in which multiple unit cells are explicitly included. While such effects can never be entirely eliminated, convergence testing allows one to determine the minimal supercell size at which they become negligible for the properties of interest.

2.5.2 Modeling Neutral Defects

In solids, defects are commonly classified according to their dimensionality. Point defects include *vacancies*, where a lattice site remains unoccupied; *substitutions*, where a lattice atom is replaced by a different species; and *interstitials*, where additional atoms occupy positions between regular lattice sites (see Figure 2.7). Defects are further categorized as intrinsic, arising from the constituent elements of the solid, or extrinsic, originating from impurities introduced by external sources. The point defects are typically denoted using the Kröger-

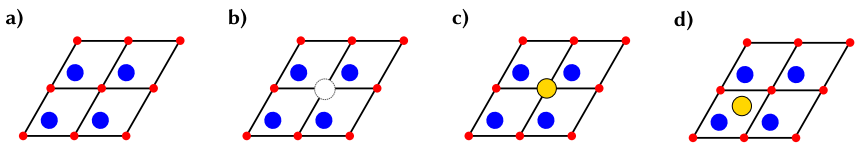

Figure 2.7: Sketches of common defect types in crystalline solids: a) the pristine structure, b) a vacancy defect, c) a substitution defect, and d) an interstitial defect.

Vink notation by X_S^q, where X is the defect species (V for vacancy), S is the lattice site (i for interstitial), and q is the charge state of the defect.[110] Extended defects, such as dislocations and grain boundaries, occur along lines or planes but are beyond the scope of this work.

Using the formalism introduced by Zhang and Northrup,[111] the defect formation energy for neutral defects is defined by

$$E_{\text{form}}^0 = E_{X_S^0} - E_0 + \sum_i n_i \mu_i \tag{2.68}$$

Here, $E_{X_S^q}$ is the total energy obtained for the defective supercell and E_0 is the total energy obtained for the pristine cell. μ_i is the chemical potential of element i, which is added to ($n_i > 0$) or removed ($n_i < 0$) from the cell. The general definition of μ is given as

$$\mu = \left(\frac{\partial G}{\partial N} \right)_{p,T} \tag{2.69}$$

where $G = U - TS + pV$ is the Gibbs free energy of the system and N is the number of particles. Accordingly, the Gibbs free energy of formation for Si_3N_4 is given as $\Delta_f G = 3\mu_{Si} + 4\mu_N$. Since high-temperature and -pressure regimes are beyond the scope of this thesis, all results are obtained using ground state DFT at 0 K without external pressure is sufficient for the defect modeling thereby fulfilling the requirement for constant p and T. Assuming further that the zero-point energy is a negligible contribution to the internal energy U compared to the electronic energy and the defect formation energies, G can be approximated by the DFT energies E^{DFT} such that

$$\mu = \left(\frac{\partial E^{\text{DFT}}}{\partial N} \right)_{p,T} \approx \frac{E^{\text{DFT}}}{N} \,. \tag{2.70}$$

For a meaningful quantification of formation energies, the reference system that represents the reservoir for the chemical potentials needs to be properly chosen. For solids, the most stable crystalline phase is usually an adequate choice yielding

$$\mu_{\text{solid}} = \frac{E_{\text{supercell}}^{\text{DFT}}}{N_{\text{atoms}}} \,. \tag{2.71}$$

For molecular dimers like $H_{2(g)}$, $N_{2(g)}$, and $O_{2(g)}$, μ is calculated analogously by

$$\mu_{\text{dimer}} = \frac{1}{2} E_{X_{2(g)}}^{\text{DFT}} \,. \tag{2.72}$$

2.5.3 Modeling Charged Defects

If the system is not electronically neutral, some additional practical aspects must be taken into account. Changing the charge state requires to include the potential μ_e associated with transferring electrons between the system and an external reservoir. Following Janak's theorem,[112] this potential corresponds to the energy level of the valence band maximum (VBM) of the reference system, such that $\mu_e = E_{\mathrm{VBM},0}$. In amorphous solids, however, defining the VBM is nontrivial since the inherent structural disorder gives rise to an extended Urbach tail of localized, occupied states extending into the band gap above the nominal valence-band edge. Consequently, there is no sharply defined VBM. A practical and physically meaningful solution is to use the mobility edge as the reference instead. The mobility edge provides a consistent and transferable energy reference across different amorphous samples, in contrast to the tail states, which are sparse in a finite-sized simulation cell and vary significantly in energy. Moreover, since the tail states are highly localized, the mobility edge offers a better correspondence to the external-reservoir interpretation of μ_e as it delineates the transition from localized to delocalized electronic states that can effectively exchange charge with the environment.

In practice, it is not straight-forward to determine the energy at which the mobility edge lies. A useful quantitative measure for the degree of localization of a state is the *inverse participation ratio* (IPR), defined as

$$\mathrm{IPR}(i) = \frac{\sum_j c_{ij}^4}{\left(\sum_j c_{ij}^2\right)^2} , \tag{2.73}$$

where c_{ij} are the coefficients of the wave function of state i. In the fully localized limit where the wave function is confined to a single atom, the IPR approaches 1. In contrast, in the completely delocalized limit it approaches $1/N$, with N being the number of atoms in the supercell. The IPR therefore provides a systematic criterion to distinguish localized from delocalized states and to estimate the mobility edge. However, extracting and evaluating all wave functions is computationally demanding. For this reason, after verifying by calculating the IPR for a few structures, the mobility edge is determined in this work from the projection of the electronic states onto atomic orbitals. States contributing approximately equally to s-, p-, and d-orbitals are considered delocalized, as the molecular orbital picture ceases to be valid in the extended solid.

Modeling charged systems raises a fundamental problem in the presence of periodic boundary conditions (PBCs): A non-neutral supercell is, by construction, surrounded by non-neutral periodic images and as a result, the long-range Coulomb energy diverges. To avoid this divergence, a uniform jellium background charge is introduced that compensates the net charge of the supercell, thereby restoring overall neutrality of the periodic system. In CP2K,[109,113] this is handled implicitly through the construction of the Hartree potential (Equation 2.33) such that it satisfies Poisson's equation.[114–117] While working well for homogeneous electron densities, the jellium approach breaks down when charges localizes on individual or a handful of atoms. Since this situation is common for point defects, especially when they give rise to localized Anderson-states, a more elaborated correction scheme is required. Therefore, the Northrup-Zhang formalism is extended for a system in the charge state q to

$$E^q_{\text{form}} = E_{\text{X}^q_\text{S}} - E_0 + \sum_i n_i \mu_i + q\,(E_\text{V} + \Delta E_\text{F}) + E_\text{corr}\ . \tag{2.74}$$

where $E_\text{V} + \Delta E_\text{F}$ is the potential alignment term and E_corr is the image charge correction.

The necessity to correct for changes in the background potential arises from the difference in the jellium background levels between the defective and reference supercells.[118] Because overall charge neutrality must be maintained regardless of the electronic charge state, the background potential in both systems shifts when the charge state is altered. The corresponding potential-alignment correction is therefore given by

$$E_\text{V} = q\Delta V_\text{pa}\ . \tag{2.75}$$

Here $V_\text{pa} = 1/2\,(V_{\text{pa,X}^q_\text{S}} - V_{\text{pa},0})$ is the average difference between the atomic-site electrostatic potential far away from the defect $V_{pa,\text{X}^q_\text{S}}$ and the reference cell $V_{\text{pa},0}$.[119] For the point-like charge distributions occurring for localized states, an additional correction is required accounting for their long-range interaction with their own periodic images. The simplest approach is to treat these localized charges as point charges, such that they can be corrected by a Madelung-type expansion derived from the screened Coulomb potential between acting between the point charges. Makov and Payne[120] extended this idea by introducing a multipole expansion

$$E^\text{MP}_\text{corr} = \frac{q^2\alpha_\text{M}}{2\varepsilon L} - \frac{2\pi qQ}{3\varepsilon L^3} + \mathcal{O}(L^{-5}) \tag{2.76}$$

with the Madelung constant α_M, the dielectric constant ε, and the quadrupole moment Q to correct for the fact that charged defects are not perfect point charges. Lany and Zunger discovered empirically, that Q itself scales with qL^2, making the second term in Equation 2.76 rather proportional to q^2/L.[121] Consequently, the $1/L$ contribution dominates and there is no major gain from the quadrupole expansion. Motivated by these findings, they modified the Madelung term (first term in Equation 2.76) by introducing a shape factor c_{sh} derived from the Wigner-Seitz cell of the supercell such that

$$E_{corr}^{LZ} = \left[1 + c_{sh}\left(1 - \varepsilon^{-1}\right)\right] \frac{q^2 \alpha_M}{2\varepsilon L} \,. \tag{2.77}$$

Since the introduction of the Lany-Zunger (LZ) correction, further efforts have been made to develop more physically motivated charge-correction schemes.[122,123] In particular, Freysoldt, Neugebauer, and Van de Walle proposed a more accurate description of the defect charge distribution by replacing point charges with Gaussian charge densities.[122] In practice, however, these more sophisticated approaches do not lead to substantial improvements in the calculated formation energies.[118] Therefore, the simple yet robust LZ charge correction is employed in this thesis.

References

[1] Cramer, C. J., *Essentials of Computational Chemistry: Theories and Models*, 2nd ed.; Wiley: Chichester, West Sussex, England; Hoboken, NJ, 2004.

[2] Jensen, F., *Introduction to Computational Chemistry*, 2nd ed.; John Wiley & Sons: Chichester, England ; Hoboken, NJ, 2007.

[3] Filot, I., *Elements of Electronic Structure Theory*; Eindhoven University of Technology: Eindhoven, 2025; Vol. 1.

[4] Sze, S. M.; Li, Y.; Ng, K. K., *Physics of Semiconductor Devices*, 4th ed.; John Wiley & Sons, Inc: Hoboken, NJ, 2021.

[5] Hunklinger, S.; Enss, C., *Solid State Physics*, 1st ed.; De Gruyter: Boston, 2022.

[6] Müller, U., *Inorganic Structural Chemistry*, 2nd ed.; Wiley: Chichester, England ; Hoboken, NJ, 2007.

[7] Winkler, H. G. F. *Naturwissenschaften* **1950**, *37*, 385–390.

[8] Pitteri, M.; Zanzotto, G. *Acta Crystallogr. A* **1996**, *52*, 830–838.

[9] Bishop, D. M., *Group Theory and Chemistry*; Dover Publications Inc.: New York, 1993.

[10] Hermann, C. *Z. Kristallogr. Cryst. Mater.* **1931**, *76*, 559–561.

[11] Mauguin, C. *Z. Kristallogr. Cryst. Mater.* **1931**, *76*, 542–558.

[12] Messier, D. R.; Riley, F. L.; Brook, R. J. *J. Mater. Sci.* **1978**, *13*, 1199–1205.

[13] Sarin, V. *Mater. Sci. Eng. A* **1988**, *105-106*, 151–159.

[14] Liang, J.-j.; Topor, L.; Navrotsky, A.; Mitomo, M. *J. Mater. Res.* **1999**, *14*, 1959–1968.

[15] Zerr, A.; Miehe, G.; Serghiou, G.; Schwarz, M.; Kroke, E.; Riedel, R.; Fueß, H.; Kroll, P.; Boehler, R. *Nature* **1999**, *400*, 340–342.

[16] Goodman, P.; O'Keeffe, M. *Acta Crystallogr. B* **1980**, *36*, 2891–2893.

[17] Du Boulay, D.; Ishizawa, N.; Atake, T.; Streltsov, V.; Furuya, K.; Munakata, F. *Acta Crystallogr. B* **2004**, *60*, 388–405.

[18] Frenkel, D.; Smit, B., *Understanding Molecular Simulation*, 2nd ed.; Academic Press: San Diego, Calif. and London, 2002; Vol. 1.

[19] Harrison, J. A.; Schall, J. D.; Maskey, S.; Mikulski, P. T.; Knippenberg, M. T.; Morrow, B. H. *Appl. Phys. Rev.* **2018**, *5*, 031104.

[20] Cohen, M. L. *Science* **1993**, *261*, 307–308.

[21] Ceder, G. *Science* **1998**, *280*, 1099–1100.

[22] Ward, L.; Agrawal, A.; Choudhary, A.; Wolverton, C. *npj Comput. Mater.* **2016**, *2*, 16028.

[23] Oganov, A. R.; Pickard, C. J.; Zhu, Q.; Needs, R. J. *Nat. Rev. Mater.* **2019**, *4*, 331–348.

[24] Mie, G. *Ann. Phys.* **1903**, *316*, 657–697.

[25] Jones, J. E.; Chapman, S. *Proc. R. Soc. Lond. A: Math. Phys. Sci.* **1924**, *106*, 441–462.

[26] Jones, J. E.; Chapman, S. *Proc. R. Soc. Lond. A: Math. Phys. Sci.* **1924**, *106*, 463–477.

[27] Jones, J. E.; Chapman, S. *Proc. R. Soc. Lond. A: Math. Phys. Sci.* **1924**, *106*, 709–718.

[28] Lennard-Jones, J. E.; Dent, B. M. *Trans. Faraday Soc.* **1928**, *24*, 92–108.

[29] Fischer, J.; Wendland, M. *Fluid Phase Equilibria* **2023**, *573*, 113876.

[30] Schwerdtfeger, P.; Wales, D. J. *J. Chem. Theory Comput.* **2024**, *20*, 3379–3405.

[31] London, F. *Z. Phys. Chem. B* **1930**, *11*, 222–251.

[32] Allen, M. P.; Tildesley, D. J., *Computer Simulation of Liquids*, 2nd ed.; Oxford University Press: Oxford, 2017.

[33] Marian, C. M.; Gastreich, M.; Gale, J. D. *Phys. Rev. B* **2000**, *62*, 3117–3124.

[34] Dasmahapatra, A.; Kroll, P. *Comput. Mater. Sci.* **2018**, *148*, 165–175.

[35] Ewald, P. P. *Ann. Phys.* **1921**, *369*, 253–287.

[36] Morse, P. M. *Phys. Rev.* **1929**, *34*, 57–64.

[37] Tsuneyuki, S.; Tsukada, M.; Aoki, H.; Matsui, Y. *Phys. Rev. Lett.* **1988**, *61*, 869–872.

[38] Stillinger, F. H.; Weber, T. A. *Phys. Rev. B* **1985**, *31*, 5262–5271.

[39] Tangney, P.; Scandolo, S. *J. Chem. Phys.* **2002**, *117*, 8898–8904.

[40] Pedone, A.; Malavasi, G.; Menziani, M. C.; Cormack, A. N.; Segre, U. *J. Phys. Chem. B* **2006**, *110*, 11780–11795.

[41] Rohskopf, A.; Seyf, H. R.; Gordiz, K.; Tadano, T.; Henry, A. *npj Comput. Mater.* **2017**, *3*, 26.

[42] Cowen, B. J.; El-Genk, M. S. *Comput. Mater. Sci.* **2015**, *107*, 88–101.

[43] Sunyer, E.; Jund, P.; Kob, W.; Jullien, R. *J. Non-Cryst. Solids* **2002**, *307-310*, 939–945.

[44] Winkler, A.; Horbach, J.; Kob, W.; Binder, K. *J. Chem. Phys.* **2004**, *120*, 384–393.

[45] Gordiz, K.; Muraleedharan, M. G.; Henry, A. *J. Appl. Phys.* **2019**, *125*, 135102.

[46] Bourova, E.; Richet, P.; Parker, S. C. *Phys. Chem. Miner.* **2004**, *31*, 569–579.

[47] Kimizuka, H.; Kaburaki, H. *Phys. Status Solidi B* **2005**, *242*, 607–620.

[48] Herzbach, D.; Binder, K.; Müser, M. H. *J. Chem. Phys.* **2005**, *123*, 124711.

[49] Van Beest, B. W.; Kramer, G. J.; van Santen, R. A. *Phys. Rev. Lett.* **1990**, *64*, 1955–1958.

[50] Sundararaman, S.; Huang, L.; Ispas, S.; Kob, W. *J. Chem. Phys.* **2018**, *148*, 194504.

[51] Sundararaman, S.; Huang, L.; Ispas, S.; Kob, W. *J. Chem. Phys.* **2019**, *150*, 154505.

[52] Buckingham, R. A. *Proc. R. Soc. Lond. A: Math. Phys. Sci.* **1997**, *168*, 264–283.

[53] Paus, H. J., *Physik in Experimenten und Beispielen*, 3rd ed.; Hanser: München, 2007.

[54] Wolf, D.; Keblinski, P.; Phillpot, S. R.; Eggebrecht, J. *J. Chem. Phys.* **1999**, *110*, 8254–8282.

[55] Carré, A.; Berthier, L.; Horbach, J.; Ispas, S.; Kob, W. *J. Chem. Phys.* **2007**, *127*, 114512.

[56] Tersoff, J. *Phys. Rev. B* **1988**, *37*, 6991–7000.

[57] Munetoh, S.; Motooka, T.; Moriguchi, K.; Shintani, A. *Comput. Mater. Sci.* **2007**, *39*, 334–339.

[58] Schrödinger, E. *Ann. Phys.* **1926**, *385*, 437–490.

[59] Born, M.; Oppenheimer, R. *Ann. Phys.* **1927**, *389*, 457–484.

[60] Thomas, L. H. *Math. Proc. Camb. Phil. Soc.* **1927**, *23*, 542–548.

[61] Fermi, E. *Z. Phys.* **1928**, *48*, 73–79.

[62] Hohenberg, P. *Phys. Rev.* **1964**, *136*, B864–B871.

[63] Kohn, W.; Sham, L. J. *Phys. Rev.* **1965**, *140*, A1133–A1138.

[64] Dirac, P. A. M. *Math. Proc. Camb. Phil. Soc.* **1930**, *26*, 376–385.

[65] Ceperley, D. M.; Alder, B. J. *Phys. Rev. Lett.* **1980**, *45*, 566–569.

[66] Perdew, J. P.; Zunger, A. *Phys. Rev. B* **1981**, *23*, 5048–5079.

[67] Perdew, J. P.; Wang, Y. *Phys. Rev. B* **1992**, *45*, 13244–13249.

[68] Perdew, J. P.; Wang, Y. *Phys. Rev. B* **2018**, *98*, 079904.

[69] Vosko, S. H.; Wilk, L.; Nusair, M. *Can. J. Phys.* **1980**, *58*, 1200–1211.

[70] Perdew, J. P.; Burke, K.; Ernzerhof, M. *Phys. Rev. Lett.* **1996**, *77*, 3865–3868.

[71] Perdew, J. P.; Burke, K.; Ernzerhof, M. *Phys. Rev. Lett.* **1997**, *78*, 1396.

[72] Sousa, S. F.; Fernandes, P. A.; Ramos, M. J. *J. Phys. Chem. A* **2007**, *111*, 10439–10452.

[73] Haas, P.; Tran, F.; Blaha, P.; Schwarz, K.; Laskowski, R. *Phys. Rev. B* **2009**, *80*, 195109.

[74] Riley, K. E.; Op't Holt, B. T.; Merz, K. M. *J. Chem. Theory Comput.* **2007**, *3*, 407–433.

[75] Perdew, J. P. *Int. J. Quantum Chem.* **2009**, *28*, 497–523.

[76] Xiao, H.; Tahir-Kheli, J.; Goddard, W. A. *J. Phys. Chem. Lett.* **2011**, *2*, 212–217.

[77] Stampfl, C.; Van De Walle, C. G. *Phys. Rev. B* **1999**, *59*, 5521–5535.

[78] Janotti, A.; Segev, D.; Van De Walle, C. G. *Phys. Rev. B* **2006**, *74*, 045202.

[79] Becke, A. D. *J. Chem. Phys.* **1993**, *98*, 5648–5652.

[80] Perdew, J. P.; Ruzsinszky, A.; Tao, J.; Staroverov, V. N.; Scuseria, G. E.; Csonka, G. I. *J. Chem. Phys.* **2005**, *123*, 062201.

[81] Adamo, C.; Barone, V. *J. Chem. Phys.* **1999**, *110*, 6158–6170.

[82] Heyd, J.; Scuseria, G. E.; Ernzerhof, M. *J. Chem. Phys.* **2003**, *118*, 8207–8215.

[83] Heyd, J.; Scuseria, G. E.; Ernzerhof, M. *J. Chem. Phys.* **2006**, *124*, 219906.

[84] Leininger, T.; Stoll, H.; Werner, H.-J.; Savin, A. *Chem. Phys. Lett.* **1997**, *275*, 151–160.

[85] Heyd, J.; Scuseria, G. E. *J. Chem. Phys.* **2004**, *121*, 1187–1192.

[86] Krukau, A. V.; Vydrov, O. A.; Izmaylov, A. F.; Scuseria, G. E. *J. Chem. Phys.* **2006**, *125*, 224106.

[87] Stowasser, R.; Hoffmann, R. *J. Am. Chem. Soc.* **1999**, *121*, 3414–3420.

[88] Foster, J. M.; Boys, S. F. *Rev. Mod. Phys.* **1960**, *32*, 303–304.

[89] Reeves, C. M.; Fletcher, R. *J. Chem. Phys.* **1965**, *42*, 4073–4081.

[90] O-ohata, K.; Taketa, H.; Huzinaga, S. *J. Phys. Soc. Jpn.* **1966**, *21*, 2306–2313.

[91] Hehre, W. J.; Stewart, R. F.; Pople, J. A. *J. Chem. Phys.* **1969**, *51*, 2657–2664.

[92] Binkley, J. S.; Pople, J. A.; Hehre, W. J. *J. Am. Chem. Soc.* **1980**, *102*, 939–947.

[93] Gordon, M. S.; Binkley, J. S.; Pople, J. A.; Pietro, W. J.; Hehre, W. J. *J. Am. Chem. Soc.* **1982**, *104*, 2797–2803.

[94] Schäfer, A.; Horn, H.; Ahlrichs, R. *J. Chem. Phys.* **1992**, *97*, 2571–2577.

[95] Hariharan, P. C.; Pople, J. A. *Theoret. Chim. Acta* **1973**, *28*, 213–222.

[96] Francl, M. M.; Pietro, W. J.; Hehre, W. J.; Binkley, J. S.; Gordon, M. S.; DeFrees, D. J.; Pople, J. A. *J. Chem. Phys.* **1982**, *77*, 3654–3665.

[97] Dunning Jr., T. H. *J. Chem. Phys.* **1989**, *90*, 1007–1023.

[98] Weigend, F.; Ahlrichs, R. *Phys. Chem. Chem. Phys.* **2005**, *7*, 3297–3305.

[99] Bloch, F. *Z. Phys.* **1929**, *52*, 555–600.

[100] Pickett, W. E. *Comput. Phys. Rep.* **1989**, *9*, 115–197.

[101] Troullier, N.; Martins, J. L. *Phys. Rev. B* **1991**, *43*, 1993–2006.

[102] Fuchs, M.; Scheffler, M. *Comput. Phys. Commun.* **1999**, *119*, 67–98.

[103] Lippert, G. R. Die GAPW-Dichtefunktional-Methode für Ab-Initio-Molekulardynamik-Simulationen, PhD Thesis, Stuttgart: University of Stuttgart, 1998.

[104] Lippert, G.; Hutter, J.; Parrinello, M. *Mol. Phys.* **1997**, *92*, 477–487.

[105] Lippert, G.; Hutter, J.; Parrinello, M. *Theor. Chem. Acc.* **1999**, *103*, 124–140.

[106] Goedecker; Teter; Hutter *Phys. Rev. B* **1996**, *54*, 1703–1710.

[107] Hartwigsen, C.; Goedecker, S.; Hutter, J. *Phys. Rev. B* **1998**, *58*, 3641–3662.

[108] Kleinman, L.; Bylander, D. M. *Phys. Rev. Lett.* **1982**, *48*, 1425–1428.

[109] Kühne, T. D. et al. *J. Chem. Phys.* **2020**, *152*, 194103.

[110] Kröger, F. A.; Vink, H. J. In *Solid State Physics*, Seitz, F., Turnbull, D., Eds.; Academic Press: 1956; Vol. 3, pp 307–435.

[111] Zhang, S. B.; Northrup, J. E. *Phys. Rev. Lett.* **1991**, *67*, 2339–2342.

[112] Janak, J. F. *Phys. Rev. B* **1978**, *18*, 7165–7168.

[113] Iannuzzi, M. et al. *J. Phys. Chem. B* **2026**, *130*, 1237–1310.

[114] Blöchl, P. E. *J. Chem. Phys.* **1995**, *103*, 7422–7428.

[115] Martyna, G. J.; Tuckerman, M. E. *J. Chem. Phys.* **1999**, *110*, 2810–2821.

[116] Genovese, L.; Deutsch, T.; Neelov, A.; Goedecker, S.; Beylkin, G. *J. Chem. Phys.* **2006**, *125*, 074105.

[117] Bani-Hashemian, M. H.; Brück, S.; Luisier, M.; VandeVondele, J. *J. Chem. Phys.* **2016**, *144*, 044113.

[118] Durrant, T. R.; Murphy, S. T.; Watkins, M. B.; Shluger, A. L. *J. Chem. Phys.* **2018**, *149*, 024103.

[119] Lany, S.; Zunger, A. *Phys. Rev. B* **2008**, *78*, 235104.

[120] Makov, G.; Payne, M. C. *Phys. Rev. B* **1995**, *51*, 4014–4022.

[121] Lany, S.; Zunger, A. *Model. Simul. Mat. Sci. Eng.* **2009**, *17*, 084002.

[122] Freysoldt, C.; Neugebauer, J.; Van de Walle, C. G. *Phys. Rev. Lett.* **2009**, *102*, 016402.

[123] Kumagai, Y.; Oba, F. *Phys. Rev. B* **2014**, *89*, 195205.